Determination of Atomic Positions from Time Resolved High Resolution Transmission Electron Microscopy Images

Zahra Hussaini[1], *Pin Ann Lin*[1,2], *Bharath Natarajan*[3,4], *Wenhui Zhu*[5], *Renu Sharma*[1*]

[1]Center for Nanoscale Science and Technology, National Institute of Standards and Technology, Gaithersburg, MD 20899-6203

[2]Maryland NanoCenter, University of Maryland, College Park, MD 20742, USA

[3]Material Measurement Laboratory, National Institute of Standards and Technology, Gaithersburg, MD 20899-6203

[4]Department of Physics, Georgetown University, Washington DC 20057, USA

[5]Department of Mechanical Engineering & Materials Science and Engineering Program, State University of New York, Binghamton, NY 13902, USA

*Corresponding Author: renu.sharma@nist.gov

Highlights

- A platform for automated image processing to determine atomic column positions from high-resolution TEM (BFTEM and STEM) images is presented.
- Interatomic distances are measured to within 7 pm to 15 pm precision from large data sets constituted of frames from *in situ* BFTEM videos.
- Application of the image processing scheme is demonstrated by quantifying atomic-scale changes in catalyst particles during CNT growth and in 2D iron oxide nanomaterials during reduction.

- Software is available for public use at https://github.com/usnistgov/tem_analysis.

Abstract

For many reaction processes, such as catalysis, phase transformations, nanomaterial synthesis etc., nanoscale observations at high spatial (sub-nanometer) and temporal (millisecond) resolution are required to characterize and comprehend the underlying factors that favor one reaction over another. The combination of such spatial and temporal resolution (up to 600 μs), while rich in information, produces a large number of snapshots, each of which must be analyzed to obtain the structural (and thereby chemical) information. Here we present a methodology for automated quantitative measurement of real-time atomic position fluctuations in a nanoparticle. We leverage a combination of several image processing algorithms to precisely identify the positions of the atomic columns in each image. A geometric model is then used to measure the time-evolution of distances and angles between neighboring atomic columns to identify different phases and quantify local structural fluctuations. We apply this technique to determine the atomic-level fluctuations in the relative fractions of metal and metal-carbide phases in a cobalt catalyst nanoparticle during single-walled carbon nanotube (SWCNT) growth. These measurements provided a means to obtain the number of carbon atoms incorporated into and released from the catalyst particle, thereby helping resolve carbon reaction pathways during SWCNT growth. Further we demonstrate the use of this technique to measure the reaction kinetics of iron oxide reduction. Apart from reducing the data analysis time, the statistical approach allows us to measure atomic distances with sub-pixel resolution. We show that this method can be applied universally to measure atomic positions with a precision of 0.01 nm from any set of atomic-resolution video images. With the advent of high time-resolution direct detection cameras, we anticipate such methods will be

essential in addressing the metrology problem of quantifying large datasets of time-resolved images in future.

1. Introduction

During last couple of decades, transmission electron microscopy has transformed from ‘a means to take pretty pictures’ to a ‘nano-laboratory’ where direct observations of atomic-scale changes occurring during the synthesis or operation of nano materials are revealed. Such observations have opened the door to allow direct measurements of nucleation and growth rates as well as reaction rates and activation energies. [1, 2] However, the atomic-scale mechanisms of some of the reaction steps, such as nucleation and phase transformation have been difficult to capture due to insufficient temporal resolution. Recent developments in image acquisition systems for transmission electron microscopes have made it possible to record atomic-resolution images of structural transformations caused by external stimuli, such as temperature and gas environment, at temporal resolutions ranging from 0.16 s to 600 μs.[3, 4] The combination of high temporal and high spatial resolution, required to reveal each reaction step, produces terabytes of image data. Fast Fourier transforms (FFTs) of a selected area of these atomic-resolution images have been successfully used for structure identification.[5] However, this method is applicable only if the structure of the entire nanoparticle changes uniformly with time and is limited to nanoparticles with diameters of more than 5 nm.[5] In order to extract the full range of information available from such atomic-scale image data, while still maintaining the time resolution, it is necessary to measure atomic positions and inter-atomic distances in each image precisely.

The concept of locating atomic positions from high-resolution images, acquired in either transmission or scanning transmission electron microscopy (TEM or STEM) mode has been

understood for a long time. Most of the methods developed for finding and measuring accurate atomic positions so far have been for STEM images where intensity broadening due to serial acquisition or longer exposure time is a big problem.[6] Recently, precision on the order of picometers has been demonstrated by averaging drift-corrected STEM images.[7] However, the image-averaging approach improves the measurement precision at the cost of time resolution, and is therefore of limited value when a sequence of images instead of a single image is required to decipher the entire reaction sequence. Identifying atomic positions from individual frames extracted from videos recorded in bright-field TEM mode, with low signal to noise (SNR) ratio, is more challenging than for high-contrast STEM images obtained by averaging. To meet this challenge, we have developed an automated image processing system (AIPS) comprising a set of algorithms to identify the atomic positions and measure the distances between nearest neighbors, with sub-pixel precision, in any number of time-resolved images. This data can then be used to quantify structural fluctuations in nanoparticles as a function of time. Here we present the abovementioned methodology and its application to measure atomic-scale structural fluctuations in a Co catalyst particle during single-walled carbon nanotube growth. The measurements show that the fluctuations in the catalyst nanoparticle and the trends in nanotube growth rates to be temporally complementary. Further, we demonstrate the breadth of applicability of this technique by using it to measure the reduction rate of iron oxide observed under an ETEM.

2. *In Situ* Time Series Acquisition and Structure Determination

An environmental transmission electron microscope, equipped with a differential pumping system,[8] monochromated field-emission electron source (FEG), image corrector and charge-coupled device (CCD camera) was used to acquire high-resolution videos. Atomic-resolution

videos of SWCNT growth were recorded using acetylene (C_2H_2) and Co_xMo_{1-x}/MgO (prepared by wet chemical methods) as carbon precursors and a catalyst-support system, respectively. Time-resolved images (frame rate of 0.1 s) of a Co catalyst particle of approximately 2.5 nm diameter were used for the measurements reported here (Movie S1). Visual analysis of the video revealed that the atomic positions within the nanoparticle were fluctuating during the period of observation. **Figure 1a** shows a typical frame extracted from an *in situ* video (Movie S1) recorded at 650 ^oC and under 0.01 Pa of flowing C_2H_2. Fast Fourier transformations (FFT) from different parts of selected images of the same particle show the co-existence of Co and cobalt carbide phases.[9, 10] However, the area occupied by each phase fluctuated with time (Movie S1), requiring each individual frame to be measured to get a reaction rate. From an FFT of the entire frame, the two known carbide phases, Co_3C and Co_2C could not be distinguished using the measured d-spacing, as Co_3C $d_{(211)}$ = 0.214 nm and Co_2C $d_{(111)}$ = 0.203 nm are too close to be unambiguously resolved (**Figure 1b**). However, from our prior experimental results, supported by DFT calculation, we know that the carbide phase, that is active for SWCNT, is Co_2C, [11] therefore we assigned the metal and carbide regions to have Co and Co_2C structures, respectively.

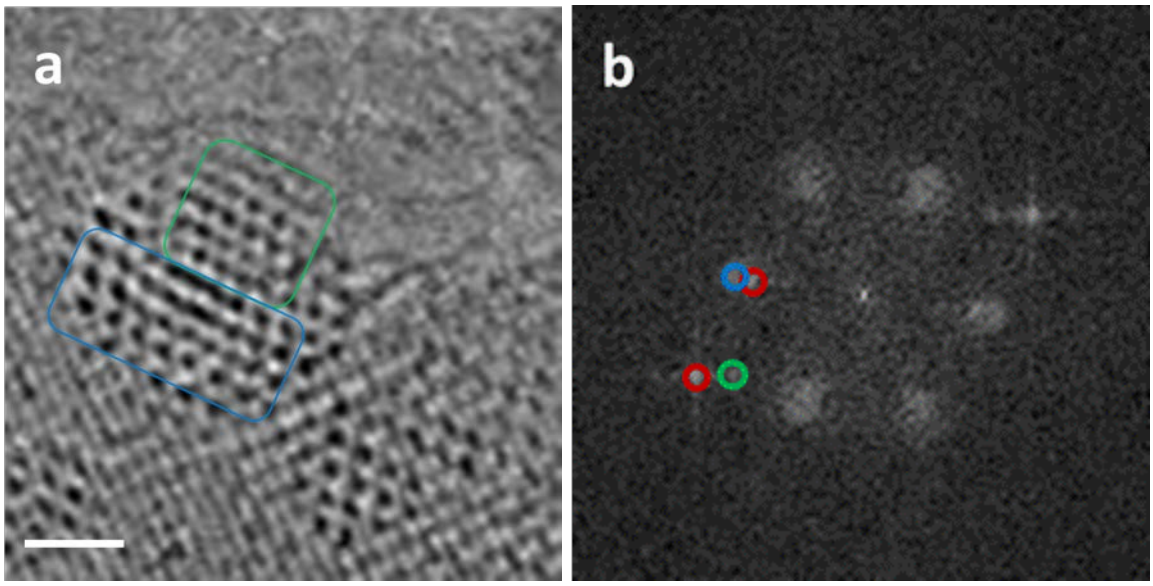

Figure 1. (a) Part of the high-resolution image extracted from the Supplementary video containing a nanoparticle active for SWCNT growth and the corresponding FFT. Red, blue and green circles enclose unique reflection from MgO, Co_2C and Co, respectively. Symmetry related reflections to the circled spots are not circled for clarity. Other spots are too broad and diffuse to distinguish between the three structures. Scale bar is 1 nm.

To confirm our image interpretation (core-shell structure of Co and Co_2C), a structure model of a 2.2 nm thick nanoparticle (**Figure 2a**), with a Co region mostly surrounded by a Co_2C shell, was generated for HRTEM image simulation using a multi-slice algorithm described elsewhere.[12] The simulated image with a sample thickness of 2.2 nm and defocus value of 9 nm (**Figure 2b**) was binned so that the pixel size (0.0457 nm) was comparable to the pixel size of the experimental images (0.0454 nm). White Gaussian noise was added to the binned image to further enhance this similarity (**Figure 3c**). The comparison between the image-analyzed simulation image and model structure was used to estimate the precision with which the algorithm can distinguish the Co from the Co_2C regions and correctly identify the boundary between them.

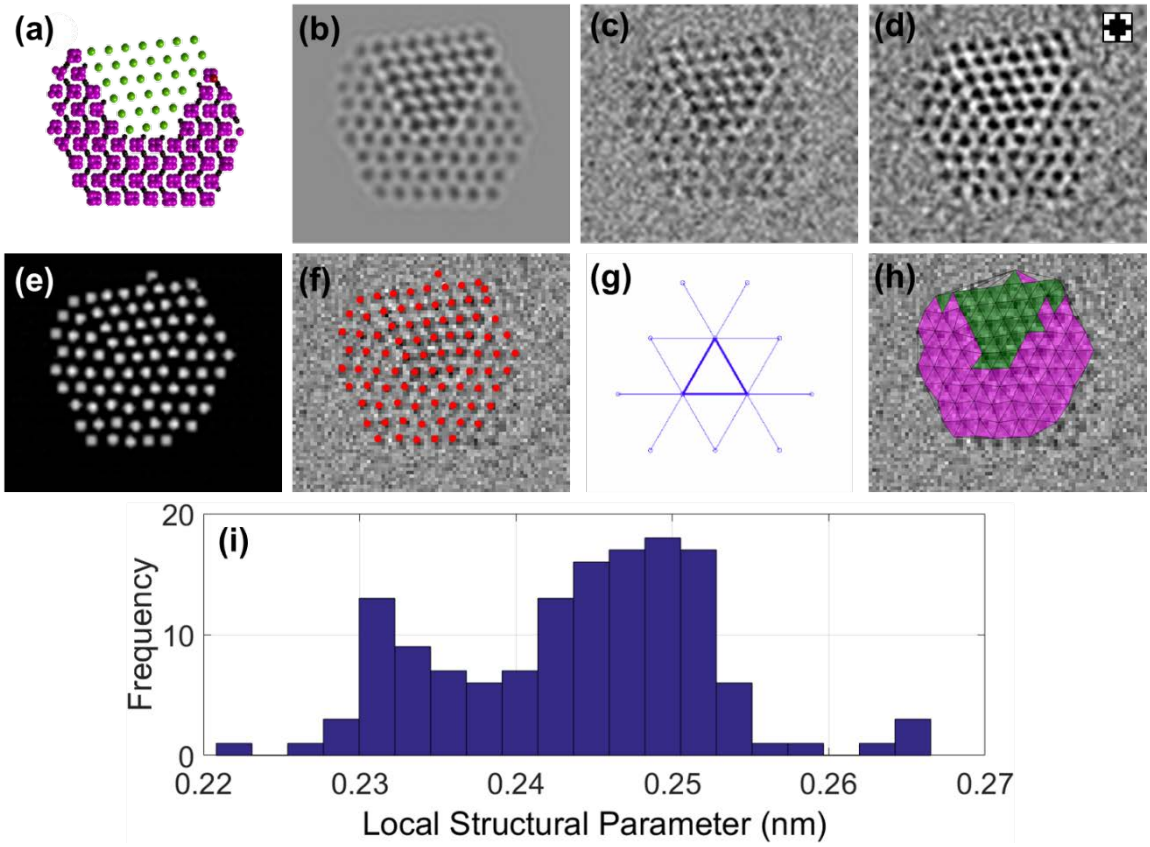

Figure 2. (a) Model nanoparticle with Co and Co_2C regions shown in green and magenta respectively. (b) Simulated image of model particle shown in (a). (c) Simulated image with added Gaussian noise. (d) Noisy simulated image after application of Weiner deconvolution. (e) Correlation image obtained by template matching using inset shown in (d). (f) Image with atomic positions identified. (g) Weighting scheme for local structural parameters (next neighbor distances): For the central triangle shown in bold, the local structural parameter is a weighted average of all distances shown. The distances shown in bold have twice the weight of the other distances. (h) The spatial distribution of triangles. Green triangles have local structural parameters below 0.24 nm and magenta triangles are above 0.24 nm. (i) Histogram of measured local structural parameters in simulated image.

Weiner deconvolution has been found to be effective in reducing peak attenuation and has been previously shown to be useful in improving SNR in noisy HRTEM images of periodic structures, such as the catalyst particle observed here.[13] This approach effectively deweights frequencies

based on the their signal-to-noise ratio. The mathematical workings of Weiner deconvolution are as follows. Given an input signal $X(i,j)$, the observed signal can be expressed in Fourier space as

$$Y(i,j) = H(i,j)X(i,j) + \eta(i,j) \quad (1)$$

where $H(i,j)$ and $\eta(i,j)$ are the Fourier transforms of the known response of the sensor and the additive noise, respectively. The goal of deconvolution is to find a $G(i,j)$ such that an estimate of the true signal may be obtained from the observed signal as follows

$$\hat{X}(i,j) = G(i,j)Y(i,j) \quad (2)$$

where $\hat{X}(i,j)$ is the estimate of the input signal $X(i,j)$ that minimizes the mean square errors between the true signal and the estimated signal. The solution to **Equation 2** is typically given by:

$$G(i,j) = \frac{H^*(i,j)}{|H(i,j)|^2 + \frac{S_\eta(i,j)}{S_X(i,j)}} \quad (3)$$

where $H^*(i,j)$ is the complex conjugate of $H(i,j)$, and $S_\eta(i,j)$ and $S_\eta(i,j)$ are the mean spectral densities of the noise and input signal, respectively, and their ratio is thus SNR. **Equation 3** therefore reduces to

$$G(i,j) = \frac{H^*(i,j)}{|H(i,j)|^2 + \frac{1}{SNR(i,j)}} \quad (4)$$

From **Equation 4** it is evident that $G(i,j)$ may be easily calculated for a known signal to noise ratio and PSF (system response). In our case, the noise was approximated to be the ratio of the mean signal to its standard deviation. The point spread function (PSF) of the imaging system, derived from the measured modulation transfer function (MTF),[14] was obtained from the vendor. The Wiener deconvolution was performed numerically. The Wiener deconvolution may

produce artificial “ringing” artifacts in the images. In the case of atomic-resolution images, ringing artifacts may appear as extra atomic columns beyond the surfaces of the nanoparticle. To reduce the influence of ringing on the analysis, a boundary was manually defined on the nanoparticle surface and only the region inside the boundary was used in further analysis. This minimizes systematic errors introduced by the deconvolution. The noise-reduced image is shown in **Figure 2d**.

2.1 Template matching

Template matching was used to highlight the positions of the atomic columns in denoised images. Template matching is a feature detection algorithm for finding small parts of an image which match a template image. The template used to find atomic columns (5 pixel × 5 pixel; 0.23 nm × 0.23 nm), was obtained by measuring the black circle approximately encapsulating an atomic column on a white background, the typical appearance of an atomic column in a HRTEM image (inset in **Figure 2d**). The template is rastered over the entire image, and at each position the correlation is calculated between the template and the part of the image that it overlaps. These correlation values create a new image, where bright spots correspond to positions which are the most likely to be atomic columns (**Figure 2e**).

2.2 Position Finding

A list of atomic column coordinates was then obtained from the correlation image by identifying individual clusters of bright pixels (i.e. atomic columns) and then calculating the centroid of each cluster. The range of the image intensities was calculated from the difference between maximum and minimum pixel intensities. A threshold intensity, *Th*, was manually set, and pixels values below *Th* were set to zero. A pixel was considered part of a cluster only if it was above the

threshold. A connected component analysis separated the image into clusters by looking for groups of pixels that were nonzero and contiguous. The position of each cluster was calculated by a weighted average of the positions of the pixels in the cluster, where the weights were the correlation values from the correlation image.

Due to the presence of false positives, an additional interactive position editor was created, which allows users to make minor adjustments to the positions of the atomic columns. The positions were compared to the original images and minor adjustments (< 5 % of atomic columns) were made to correct wrongly identified atomic column positions. The manual adjustments were repeated by multiple people in order to reduce human bias. The image with the atomic column positions identified is shown in **Figure 2f**.

2.3 Image Registration

Once the atom positions were identified it was essential to align (register) the time-stack of image files with a sub-pixel accuracy for faithful characterization of the change in atom positions with time. This was achieved by implementing a sub-pixel registration algorithm reported by Thevenaz *et al*. using ImageJ's 'stackreg' plugin.[15] The goal of this algorithm is to identify a transformation matrix T which when applied to the image $\hat{X}_j$ agrees with the reference image $\hat{X}_{j-1}$. This "agreement" was reached by minimizing the integrated square difference in the unaltered pixel intensity values between $\hat{X}_{j-1}$ and $T\hat{X}_j$ using a modified Marquart-Levenberg algorithm. The alignment was improved iteratively using a coarse-to-fine multilevel strategy (pyramid approach), thereby helping achieve sub-pixel accuracy. The alignment process was then propagated through the entire stack from $\hat{X}_0$ to $\hat{X}_N$ using each $\hat{X}_{j-1}$ as the reference to which the next slice $\hat{X}_j$ is aligned. The transformation may be rigid or non-rigid based on the imaging method and application. Non-

rigid registration is more computationally intensive and primarily required when image distortions due to probe instabilities and sample drift are prevalent. These artifacts are mainly observed when imaging in STEM mode.[7] Since we image our samples using parallel beam HRTEM, we employ rigid-body registration which only accounts for in-plane rotational and translational transformations. The registration was performed on the correlation images, such as in **Figure 3f**, as this was found to be more stable than registering the *in situ* TEM images directly. The transformation matrix used to register each frame of the correlation image series was saved, so that the same registration could be applied to the original image series and also to the point sets obtained in the position finding step.

2.5 Geometric Modeling

In order to quantify the local geometry around each atomic column, the widely-employed Delaunay triangulation method [16] was used to connect each atomic column to its nearest neighbors. The Delaunay method maximizes the minimum angle of all the angles of the triangles in the triangulation and avoids skinny or obtuse angled triangles. In practice, this produces triangulations where each feature of interest is connected to its first coordination shell. However, at the edges of the nanoparticle, where some atomic columns do not have complete coordination shells, skinny triangles do form, as seen in **Figure 2h**. These spurious triangle edges could be removed by deleting all edges longer than twice the expected interatomic distances in the nanoparticle. For each triangle, a local structural parameter i.e. the local inter-atomic column distance, was calculated and used to assign the structure of that particular triangular region of the nanoparticle. The local structural parameter is a weighted average of interatomic distances (triangle edges) over a small area, shown in **Figure 2g**.

From the model nanoparticle (**Figure 2a**), the inter-atomic column distances of the ideal Co and Co_2C structures were measured to be (0.23±0.07) nm and (0.25±0.15) nm, respectively. A histogram of the calculated inter-atomic distances from the simulated image shows two peaks centered very close to 0.23 nm and 0.25 nm, corresponding to the Co region and carbide region of the nanoparticle, respectively (**Figure 2i)**. There is therefore, a good agreement between the known atomic positions of the model particle and AIPS determined distances derived from simulated measurements. **Figure 2h** shows the spatial distribution of the triangles associated with each phase. Here too, we find good agreement between the model nanoparticle (**Figure 2a**) and the two structures, identified by the image processing scheme (**Figure 2h**), thereby suggesting that the algorithm is successful in its task.

3. Application to Experimental Data

3.1 Cobalt Catalysis

Having successfully tested the AIPS on simulated data, it was applied to the ETEM image sequence of SWCNT growth (Movie S1).[9] **Figure 3a** shows a histogram of all the local structural parameters for all the triangles in the image sequence. The histogram shows two peaks, centered at 0.23 nm and 0.25 nm. The peak at 0.25 nm is broader, and likely contains both Co_3C and Co_2C components. Individual Co_3C and Co_2C peaks could not be isolated as the measured nearest-neighbor atomic distances, 0.25 nm (Co_2C) and 0.26 nm (Co_3C), were within the measurement error. This implied that these two cobalt carbides could not be distinguished unambiguously in the image sequence as well. Consequently, the overall bimodal distribution (red) was fit by a linear combination of two Gaussian distributions centered at 0.22 nm and 0.25 nm shown as the green and magenta curves. As per the formalism defined by Bals *et al*.,[17] we calculate the precision of our measurements of the individual structural parameters to be the standard deviations of the two

Gaussian fits. The Co Gaussian fit was found to have a standard deviation of 0.007 nm (7 pm). The Co_2C Gaussian fit was found to have a standard deviation of 0. 015 nm (15 pm). It is important to note that the measurement precision is partly dependent on the point spread function (PSF) of the camera and is expected to improve as the PSF of cameras improve.

With that in mind, the histogram was used to divide the nanoparticle into cobalt metal and cobalt carbide regions. **Figure 3b** shows a typical frame from this analysis. The area of the cobalt metal and cobalt carbide regions of the nanoparticle were approximated as the area of the triangles from the triangulation. The area of cobalt metal as a fraction of the total nanoparticle area as a function of time was calculated. If the nanoparticle is spherical and that the metal region in its center is also spherical, the metal volume fraction of the nanoparticle is the area fraction raised to the 3/2 power. The volume of the Co_2C region can therefore be obtained as the volume of particle minus volume of Co region. Given that the volume of the Co_2C unit cell is 0.056 nm^3, the total number of unit cells can be calculated as the volume of the Co_2C region divided by 0.056 nm^3. Assuming that only the Co_2C shell contains the carbon atoms, and given that there are 2 carbon atoms per Co_2C unit cell, the number of carbon atoms in the particle in every frame can be calculated as 2 times the number of Co_2C unit cells in the particle.

Having determined the evolution of the carbon content in the nanoparticle, we can correlate it with the carbon nanotube growth. Since the SWCNT has a fixed diameter (d = 1.78 nm) and a regular shape, knowing the areal density of carbon on a graphene sheet (38 carbon nm^2), the number of carbon atoms in SWCNT in each frame (N_{CNT}) can be calculated from the arc length of the SWCNT profile (a) in the TEM image as

$$N_{CNT} = n\pi d\left(\frac{d}{2}+\frac{a}{2}-\frac{\pi d}{4}\right) \quad (5)$$

Where the area density of carbon in nanotube is = 38 nm^{-2}.

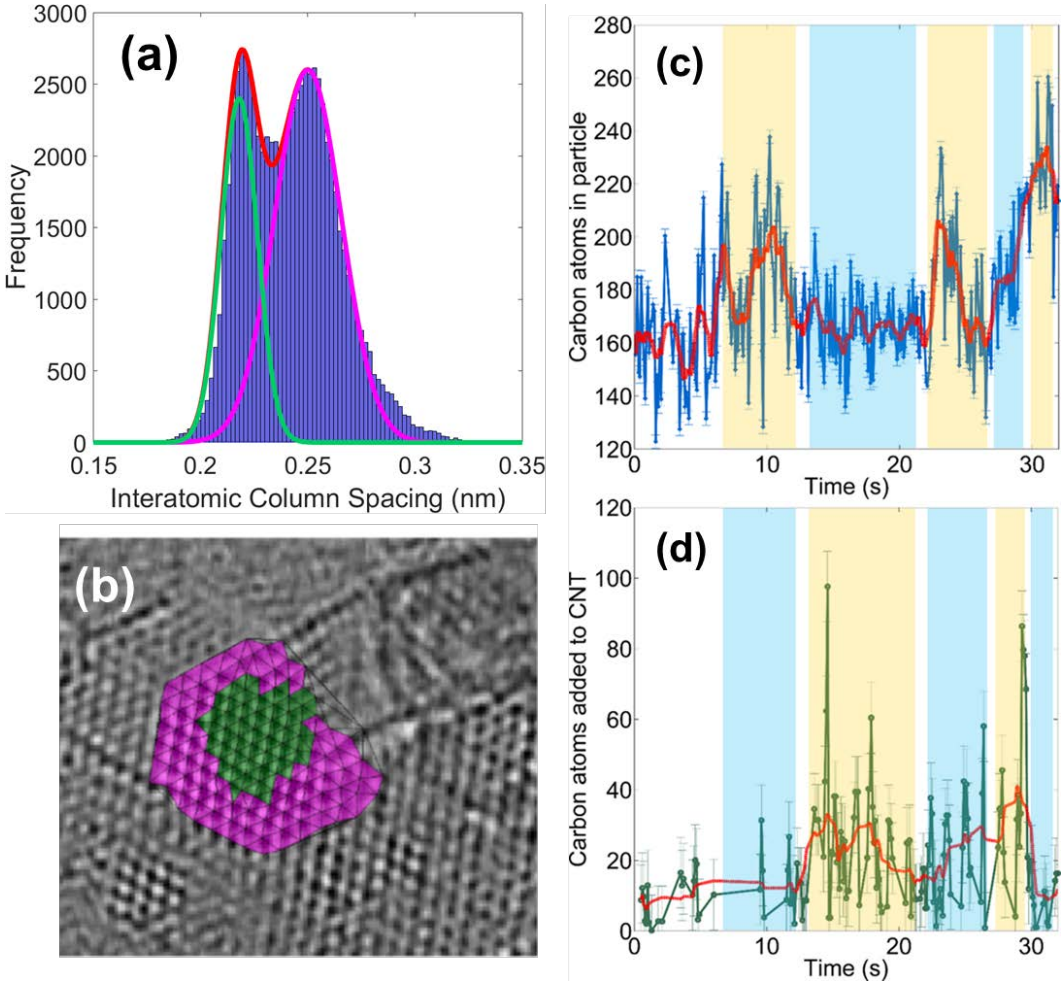

Figure 3: (a) Histogram of local structural parameters for all triangles in all frames of the video showing a bimodal distribution of interatomic spacings. The fit to the bimodal distribution is calculated to be a sum of two Gaussian distributions centered at 0.22 nm and 0.25 nm corresponding to Co (green) and Co_3C (magenta) respectively. (b) A typical size-thresholded image. The image was thresholded at 0.23 nm (shoulder in histogram in Figure 4a). Green triangles are below the threshold and magenta triangles are above the threshold. (c) Number of carbon atoms in the catalyst particle and (d) the number of carbon atoms added to growing nanotube plotted as a function of time. The red lines through the plots show a moving average of 10 frames. The periods of higher and lower carbon content are color coded as blue and yellow, respectively, simply to emphasize the anti-synchronous nature of the two reactions as confirmed by simulations reported in ref. 9.

Using the calculated values, the fluctuation in the number of carbon atoms in the particle is compared with the number of carbon atoms added to the particle. Both the carbide and the SWCNT growth fluctuations are shown in **Figure 3c-d**. The minima and maxima of the two plots are anticorrelated in time. When the amount of carbon in the nanoparticle is at a maximum the SWCNT growth is low. When these carbon atoms are let go of, the SWCNT growth is high. This suggests that the carbide in the nanoparticle decomposes and moves into the nanotube [9]. However, from our experiments we do not measure perfect anti-synchrony. We note that the correlation coefficient between the experimental values of two reaction rates is -0.18, while the simulated value was determined to be -0.92.[9] We attribute this moderate correlation coefficient to the inherently noisy nature of this data, due to various other stochastic processes, such as precursor decomposition, also occurring that effect both the carbide formation and nanotube growth.

3.2 Reduction Pathways in Iron Oxide.

The AIPS developed here was also employed to probe the dynamics of H_2-induced reduction of 2D Fe_3O_4 nanostructures observed using an environmental TEM. **Figure 4a** shows an image extracted from an *in situ* HRTEM video. The diffractograms of the two regions in **Figure 4b** show the Fe_3O_4 region converting to FeO, with the crystallographic orientation of Fe_3O_4 <111> ∥ FeO <111>. The AIPS was used to obtain structural information from each frame extracted from reduction videos recorded at 500 °C in 0.5 Pa hydrogen pressure.[18] The data was thresholded to highlight only the Fe_3O_4 phase. The triangulated atomic positions in the Fe_3O_4 areas, identified by the AIPS in **Figures 4a-b**, are shown in **Figures 4c-d**. The FeO regions are not shown. Summing the area under all acute angled triangles (the skinny triangles are spurious), the area of Fe_3O_4 in

each frame was calculated and plotted with time. (**Figure 4e**). The time dependence of Fe_3O_4 area was then used to obtain the reaction rate (the slope of the fitting of the curve: (0.48±0.03) nm^2 s^{-1}.[18] The linear time dependence of the reduction of Fe_3O_4 to FeO observed in the ETEM experiment

suggested that the reduction was a surface reaction limited process, due to the surface adsorption of H_2 molecules or the removal of H_2O.

4. Conclusions

We have developed an automated image processing system (AIPS) for determining the precise atomic positions in HRTEM images by combining publicly available and custom codes. It has been successfully applied to large experimental data sets recorded using a CCD camera at a frame rate up to 10 s^{-1}. With the AIPS we have determined atomic positions with a sub-pixel precision of 7 pm. Since the confidence and significance accuracy of the measurements will depend on the quality of the images, we believe that the precision may be improved by addressing instrumental constraints like sample drift, SNR, DQE, and PSF, which are minimized in new direct-detection high-speed cameras. From the analysis of the data generated by the AIPS we have resolved novel carbon reaction pathways in Cobalt catalyzed CNT growth and the reduction mechanisms in 2D iron oxide nanomaterials. The program is available for public use at https://github.com/usnistgov/tem_analysis. With the advent of high time-resolution direct detection cameras and associated terabyte sized imaging data, we believe our AIPS will be key to quantifying atomic-scale fluctuations and resolving novel reaction pathways.

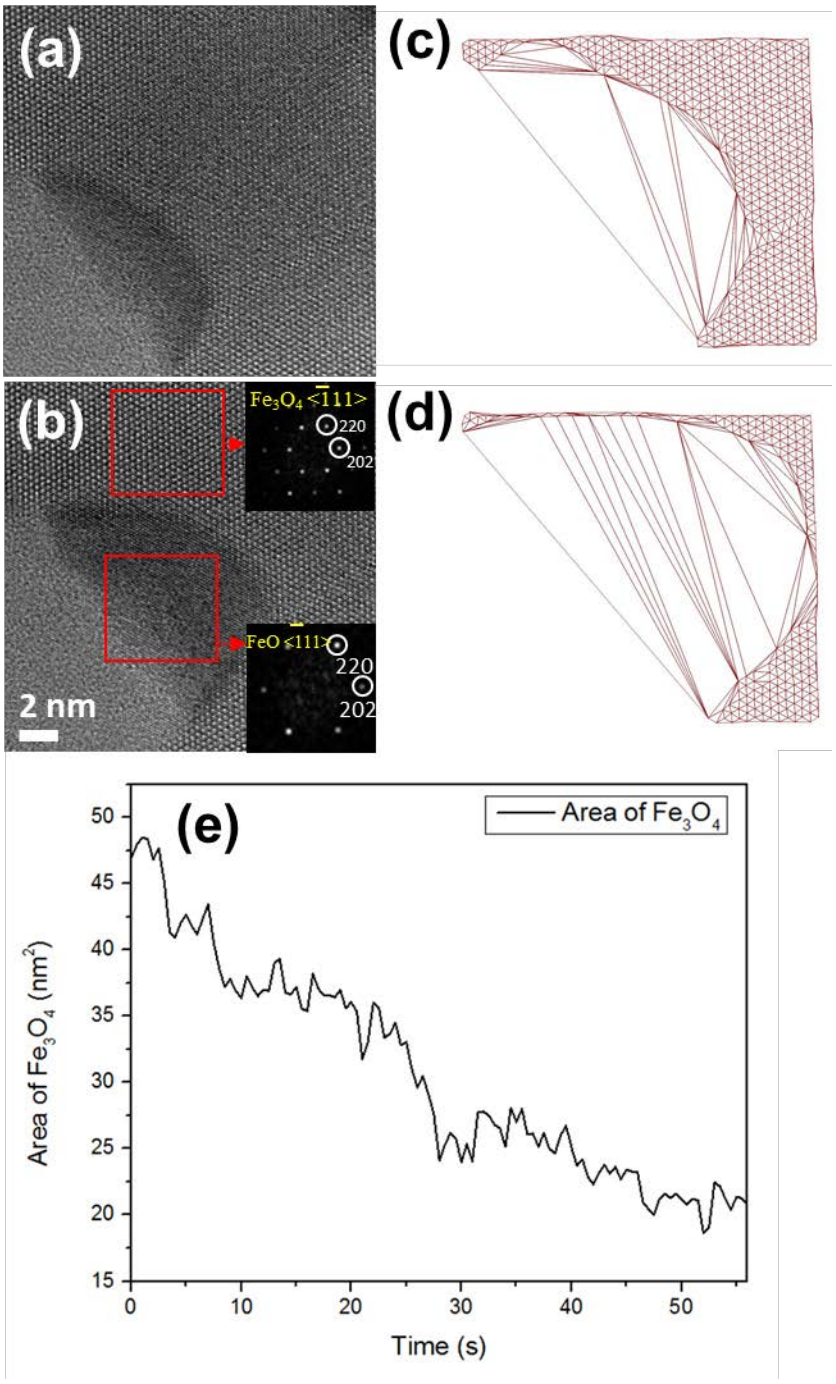

Figure 4. Reduction of Fe_3O_4 to FeO at 500 °C in 0.5 Pa of flowing H_2. (a) Frame extracted from a video after reduction has started; (b) frame extracted after 50 s (c) and (d) corresponding images extracted from AIPS where the center and the length of triangles represent Fe atomic positions and atomic distances in Fe_3O_4, the skinny triangles with large next neighbor distances show the regions of metallic Fe and were not used for measuring the reduction rate. (e) the change in number of atoms in Fe_3O_4 area measured from each frame was used to get reduction rate. [17]

Acknowledgements:

Funding from Cooperative Research Agreement (CRA) between the University of Maryland and the National Institute of Standards and Technology (NIST) (grant 70NANB10H193) (for P. A. Lin and B. Natarajan) and National Science Foundation (for W. Zhu) under NSF CAREER Award Grant CMMI-1056611) is gratefully acknowledged. We are also thankful to Wesley Griffin (NIST) John Hagedorn (NIST) and Tomasz Benarz (CSIRO) for their contributions in developing the software.

Supplementary videos:

Movie S1: High resolution video of SWCNT growth from Co catalyst supported on MgO, recorded at a frame rate of 10 s-1 at 650 C in 0.01 Pa of C_2H_2.

Movie S2: Magnified video images after AIPS. Colors represent the nearest neighbor distances (represented by the triangles in the images). Blue and magenta colors represent atomic distances corresponding to Co and cobalt carbide phase, respectively.

References

1. Gai, P.L., R. Sharma, and F.M. Ross, *Environmental (S)TEM studies of gas-liquid-solid interactions under reaction conditions.* Mrs Bulletin, 2009. **33**(2): p. 107-114.
2. Sharma, R., *Kinetic measurements from in situ tem observations.* Microscopy Research & Technique, 2008. **72**(3): p. 144-152.
3. Panciera, F., Chou, Y.-C., Reuter, M. C., Zakharov, D., Stach, E. A., Hofmann, S., Ross, F. M. , *Synthesis of nanostructures in nanowires using sequential catalyst reactions.* Nature Materials, 2015. **14**: p. 820-825.
4. Park, J., et al., *3D structure of individual nanocrystals in solution by electron microscopy.* Science, 2015. **349**(6245): p. 290-295.
5. Deruijter, W.J., et al., *Measurement of Lattice-Fringe Vectors from Digital Hrem Images - Experimental Precision.* Ultramicroscopy, 1995. **57**(4): p. 409-422.
6. den Dekker, A.J., et al., *Estimation of unknown structure parameters from high-resolution (S)TEM images: What are the limits?* Ultramicroscopy, 2013. **134**: p. 34-43.

7. Yankovich, A.B., et al., *Picometre-precision analysis of scanning transmission electron microscopy images of platinum nanocatalysts.* Nature Communications, 2014. **5**.
8. Sharma, R., *An environmental transmission electron microscope for in situ synthesis and characterization of nanomaterials.* Journal of Materials Research, 2005. **20**(7): p. 1695-1707.
9. Lin, P.A., et al., *Direct evidence of atomic-scale structural fluctuations in catalyst nanoparticles.* Journal of Catalysis, 2017. **349**: p. 149-155.
10. Gomez-Ballesteros, J.L., et al., *Nanocatalyst shape and composition during nucleation of single-walled carbon nanotubes.* Rsc Advances, 2015. **5**(129): p. 106377-106386.
11. Picher, M., et al., *Nucleation of Graphene and Its Conversion to Single-Walled Carbon Nanotubes.* Nano letters, 2014. **14**(11): p. 6104-6108.
12. Stadelmann, P.A., *EMS- A Software Package for Electron Diffraction Analysis and HREM Image Simulations in Materials Science.* Ultramicroscopy, 1987. **21**: p. 131-146.
13. Marks, L.D., *Wiener-filter enhancement of noisy HREM images.* Ultramicroscopy, 1996. **62**(1-2): p. 43-52.
14. Meyer R.R., K.A.I., Dunin-Borkowski R.E. and Hutchison J.L., *Experimental characterisation of CCD cameras for HREM at 300 kV.* Ultramicroscopy, 2000. **85**(1): p. 9-13.
15. Thevenaz, P., U.E. Ruttimann, and M. Unser, *A pyramid approach to subpixel registration based on intensity.* Ieee Transactions on Image Processing, 1998. **7**(1): p. 27-41.
16. de Berg, M., et al., *Delaunay triangulations: height interpolation.* Computational Geometry: Algorithms and Applications, 2008: p. 191-218.
17. Bals, S., et al., *Annular dark field imaging in a TEM.* Solid State Communications, 2004. **130**(10): p. 675-680.
18. Zhu, W.H., et al., *In Situ Atomic-Scale Probing of the Reduction Dynamics of Two-Dimensional Fe2O3 Nanostructures.* Acs Nano, 2017. **11**(1): p. 656-664.